Broadband Trailing-Edge Noise Reduction Using Permeable Metal Foams

Merino Martinez, Roberto; Rubio Carpio, Alejandro; Avallone, Francesco; Ragni, Daniele; Snellen, Mirjam; van der Zwaag, Sybrand

Citation (APA)
Merino Martinez, R., Rubio Carpio, A., Avallone, F., Ragni, D., Snellen, M., & van der Zwaag, S. (2017). Broadband Trailing-Edge Noise Reduction Using Permeable Metal Foams. In *Proceedings of the 46th International Congress and Exposition on Noise Control Engineering Taming Noise and Moving Quiet: Taming Noise and Moving Quiet, 27-30 Aug 2017 Hong Kong, China* (pp. 4373-4383)

Important note
To cite this publication, please use the final published version (if applicable).
Please check the document version above.

Broadband Trailing Edge Noise Reduction Using Permeable Metal Foams

Alejandro RUBIO CARPIO[1]; Roberto MERINO MARTÍNEZ[2]; Francesco AVALLONE[3]; Daniele RAGNI[4]; Mirjam SNELLEN[5]; Sybrand VAN DER ZWAAG[6]

[1,3,4]Aerodynamics, Wind-Energy, Flight Performance and Propulsion (AWEP) Department

[2,5]Aircraft Noise & Climate Effect (ANCE) Department

[6]Aerospace Structures and Materials (ASM) Department

Faculty of Aerospace Engineering, Kluyverweg 1, 2629HS

[1,2,3,4,5,6]Delft University of Technology, The Netherlands

ABSTRACT

Far-field noise measurements over a NACA 0018 airfoil with both solid and porous trailing edges, manufactured with topologically characterized metal foams, are carried out at chord-based Reynolds numbers ranging from 2.71×10^5 to 5.4×10^5 and 3 different angles of attack ranging from -0.3º to 6.8º. Three metal foams, with cell diameters of 450, 580 and 800 μm, and a similar inner structure are tested. Porous trailing edges with extension equal to 10% and 20% of the chord are investigated. Measurements of the flow parameters describing the porous media, i.e. air flow permeability and form coefficient, are additionally carried out. Far-field noise measurements are performed with a microphone phased array. In addition, the aerodynamic forces acting on the airfoil are monitored to assess the effects of the porous extension.

It is found that, at low frequency, noise attenuation with respect to the solid trailing edge configuration is reduced by increasing the angle of attack (up to 5 dB). On the other side, at higher frequencies, a larger noise reduction is measured (up to 18 dB). The dependence of the noise reduction on the angle of attack is more relevant in presence of materials with lower flow resistivity and larger cell size. Finally, it is shown that, at lower velocities, increasing the extension of the porous insert increases the noise reduction in the low frequency range.

Keywords: aeroacoustics, trailing edge noise, porous materials, noise reduction

1. INTRODUCTION

Turbulent trailing edge noise is generated when turbulent structures arising within the turbulent boundary layer are convected over the sharp trailing edge of an airfoil (1). This aeroacoustic mechanism is of paramount importance for the wind turbine industry since it is the main contributor to the overall noise generated by modern wind turbines (2). For this reason, passive and active noise reduction techniques such as the aeroacoustic optimization of the airfoil shape (3), the use of trailing edge serrations (4) or trailing edge brushes (5) have been considered to mitigate the noise generation at the source. In this manuscript, the noise scattered in presence of a porous trailing edge is investigated.

Previous literature (6,7) showed that a porous trailing edge might reduce the scattered noise because of:

- viscous damping of the acoustic pressure fluctuations;
- change in the turbulent boundary layer mean flow field;

---

[1] PhD student, a.rubiocarpio@tudelft.nl (Corresponding author)
[2] PhD student, r.merinomartinez@tudelft.nl
[3] Assistant professor, f.avallone@tudelft.nl
[4] Assistant professor, d.ragni@tudelft.nl
[5] Associate professor, m.snellen@tudelft.nl
[6] Full professor, s.vanderzwaag@tudelft.nl

- reduction of the amplitude and/or spanwise coherent length of the surface pressure fluctuations;
- balancing of the dynamic pressure mismatch between suction and pressure side at the trailing edge.

A study (7) on a fully porous SD7003 airfoil, manufactured with different porous materials, reported a reduction of the trailing edge noise exclusively in the low and medium frequency range. On the other hand, at high frequency a noise increase was ascribed to the higher surface roughness of the porous material. The noise reduction capabilities were also found to be highly dependent on the porous material properties, e.g., the air flow resistivity and the porosity. Additionally, a reduction of the aerodynamic efficiency was reported. Experiments on a partially porous SD7003 airfoil with different porous extents (8) confirmed the trends measured for the fully porous airfoils. A decrease in lift with respect to the solid airfoil was reported for lower flow resistivity or higher stream-wise extension of the porous material. Furthermore, it was found that a larger extent of porous material led to higher noise attenuation with respect to the solid case, although without specification on the frequency range.

Herr et al. (9) recently performed noise measurements in presence of a DLRF16 airfoil with a porous trailing edge covering 10% of the chord. This study further confirmed the reduction of the aerodynamic performance of the airfoil with a porous trailing edge. They measured larger noise reduction at low frequency in presence of porous trailing edge with low flow resistivity. On the other hand, the noise increase at high frequency was found to be larger for increasing pore size.

To the authors knowledge, the effect of the angle of attack on the scattered far-field noise is still not clear. Previous studies showed different results, probably due to the fact that the results were obtained using porous materials with very different microstructures or to the different experimental set-up. So far, an increase (7), a decrease (9) or a non-linear dependence (10) of the noise reduction for increasing angle of attack have been reported.

This manuscript reports far-field noise measurements of a NACA0018 airfoil with experimentally characterized porous trailing edge for different free stream velocity and angles of attack. The effect of the porous extension is further investigated.

2. EXPERIMENTAL SET-UP

2.1 Porous Materials

Three different porous NiCrAl foams with cell diameters d_c of 450 µm, 580 µm and 800 µm (figure 1) are investigated. The metal foams, which are manufactured by Alantum, have an open-cell structure. They are characterized in terms of porosity (φ), permeability (K), the form coefficient (C) and the flow resistivity (R).
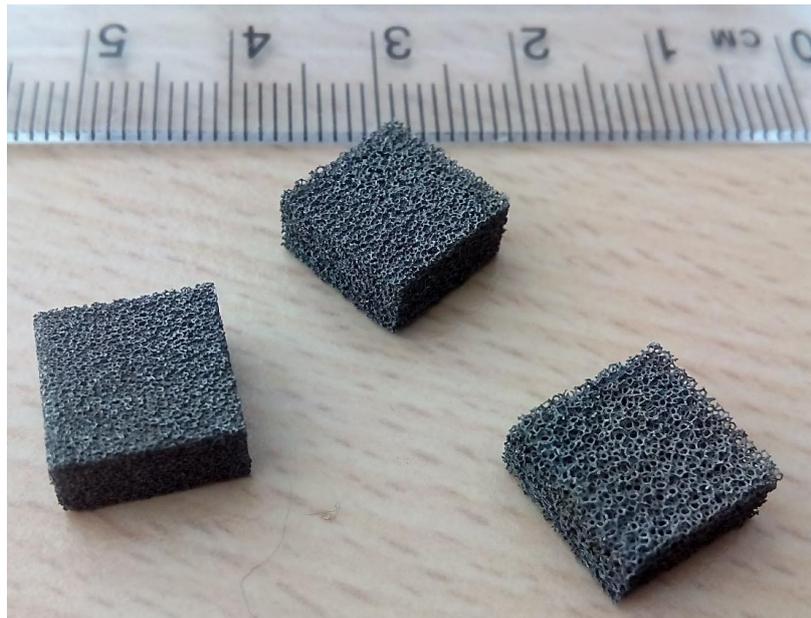
Figure 1 – Example of 10×10×5 mm³ samples of the metal foams. From left to right, the cell size of the material is 450 µm, 580 µm and 800 µm, respectively.

2.2 Porous Material Properties

The porosity of the metal foam is defined as:

$$\varphi = 1 - \frac{\rho_p}{\rho_b} \tag{1}$$

where ρ_p and ρ_b are the density of the porous and the base material, respectively. The density of the porous foam is calculated as the ratio between the weight and the volume of the $10 \times 10 \times 5$ mm^3 samples shown in figure 1. The samples are weighted using a Mettler ToledoAB204S analytical balance.

The density of the base material is retrieved from its composition, which is obtained by performing energy-dispersive X-ray spectroscopy (EDS) on the same samples used to calculate ρ_p. The EDS analysis is carried out employing a Jeol JSM-7500F Field Emission Scanning Electron Microscope.

The permeability and form coefficient are obtained from least-squares fitting of Hazen-Dupuit-Darcy equation (11):

$$\frac{\Delta p}{t} = \frac{\mu}{K} v_d + \rho C v_d^{\ 2} \tag{2}$$

where ρ is the fluid density, μ is the dynamic viscosity, $v_d = Q/A$ is the Darcian velocity, Q is the volumetric flow rate, A the cross-section area of the sample, and t is the material thickness.

In order to measure the above mentioned quantities, an experimental rig consisting of a 1.5 m long pipe is employed. The pressure drop is measured from two pressure taps placed 5 cm upstream and downstream of the test section. The test section consists of an aluminium cylinder, where 5.5 cm diameter metal foam disks are inserted. Previous research (12) showed that the permeability and form coefficient depend on the thickness of the sample until a critical thickness, which depends on the material. As a consequence, up to six 10 mm thick disks are stacked into the aluminium cylinders such to study the effect of the material thickness.

The rig is supplied by a 10 bar pipeline. The volumetric flow rate is controlled using an Aventics pressure regulator and measured by a TSI 4040 volumetric flow meter located upstream the pipe. The pressure drop is measured using a Mensor 2101 differential pressure sensor connected to the pressure taps.

The air flow resistivity is defined as:

$$R = \frac{\Delta p}{t \cdot v_d} \tag{3}$$

In order to retrieve R, the Darcian velocity v_d has to be low enough to neglect the inertial effects. In the present investigation, the air flow resistivity R is estimated as:

$$R = \frac{\mu}{K} \tag{4}$$

The measured quantities are reported in section 5.1.2.

3. Wind Tunnel and Model
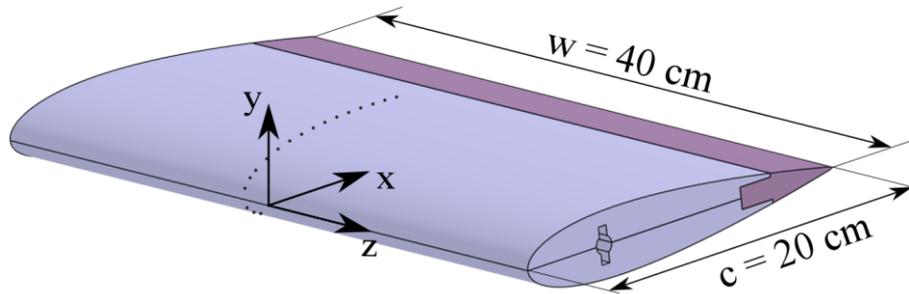
Figure 2 – Sketch of the NACA 0018 airfoil with the porous insert. The aluminum body is represented in grey while the metal foam insert is depicted in purple.

The experiments are performed in the anechoic vertical open-jet wind tunnel (V-Tunnel) at Delft University of Technology. It has a contraction ratio of 15:1 and it can be operated at a free-stream velocity up to 42.5 m/s. The rectangular test section is 40×70 cm^2. The turbulence intensity is below 0.1% for entire range of operative velocities. The free-stream velocity distribution across the test section is uniform within 0.5 %.

A NACA 0018 airfoil (figure 2), with chord c and span w lengths of 20 cm and 40 cm, respectively, is installed between two 1.2 m long side plates to guarantee two-dimensional flow (figure 3). The airfoil is located 50 cm away from the contraction exit.

The airfoil is manufactured with CNC machining from a solid aluminum plate with exchangeable trailing edges to allow the testing of different porous materials, as well as the reference (solid) configuration. The porous trailing edge inserts are manufactured using wire-cutting EDM.

Turbulent boundary-layer transition is forced at $x/c = 0.2$ at both suction and pressure sides with carborundum particles of 0.84 mm diameter randomly distributed on a 10 mm strip.

Static pressure measurements were obtained through 30 pressure orifices of 0.4 mm diameter equally distributed between the suction and the pressure sides. They are distributed along the chord-wise direction within the range $0.01 \leq x/c \leq 0.66$. The pressure taps are tilted 15° with respect to the symmetry plane of the airfoil to avoid interference. In order to measure the aerodynamic lift 15 differential pressure Honeywell TruStability HSCDRRN025MDAA3 transducers are used. Data are recorded at a sampling frequency of 2 kHz for 10 s.

The wind tunnel is operated at free-stream velocities equal to U_∞ = 20, 30 and 40 m/s, corresponding to chord-based Reynolds numbers of 2.72×10^5, 4.07×10^5 and 5.4×10^5. For each velocity, the airfoil is set at three geometrical angles of attack $\alpha_g = 0°$, $6°$ and $12°$. The effective angle of attack (α) is obtained following Brooks et al. (1) and further verified by comparing the measured surface pressure distribution with the one given by XFOIL (13). For each flow configuration, two different porous trailing edge inserts with length equal to 10 and 20 % of the chord are investigated.
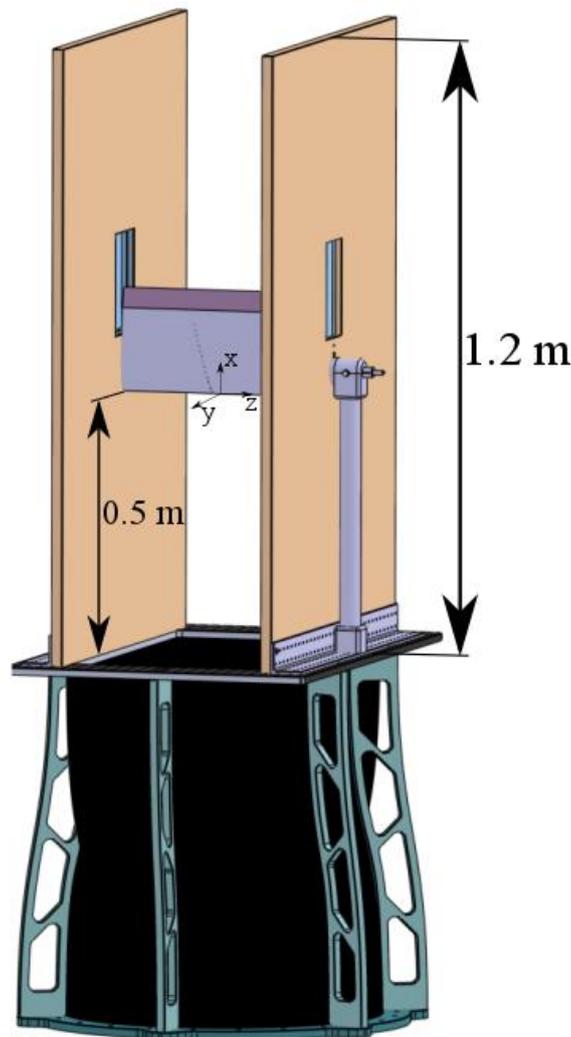
Figure 3 – CAD of the contraction and the test section with the NACA 0018 airfoil mounted.

4. Phased Microphone Array Set-Up and Data Processing

The use of phased microphone arrays and beamforming algorithms allow for the estimation the location and strength of sound sources. In this experiment, a phased microphone array consisting of 64 G.R.A.S. 40PH free-field microphones with integrated CCP preamplifiers is employed for measuring the far-field noise emissions of the airfoil trailing edge. The distribution of the microphones is an adapted Underbrink design (14,15) with 7 spiral arms of 9 microphones each, and an additional microphone located at the center of the array (figure 4 a). The diameter of the array is approximately 2 m and the distance from the array plane to the airfoil trailing edge (for $\alpha_g = 0°$) is 1.43 m. The center of the array is approximately aligned with the center of the airfoil trailing edge.

(a)   (b)
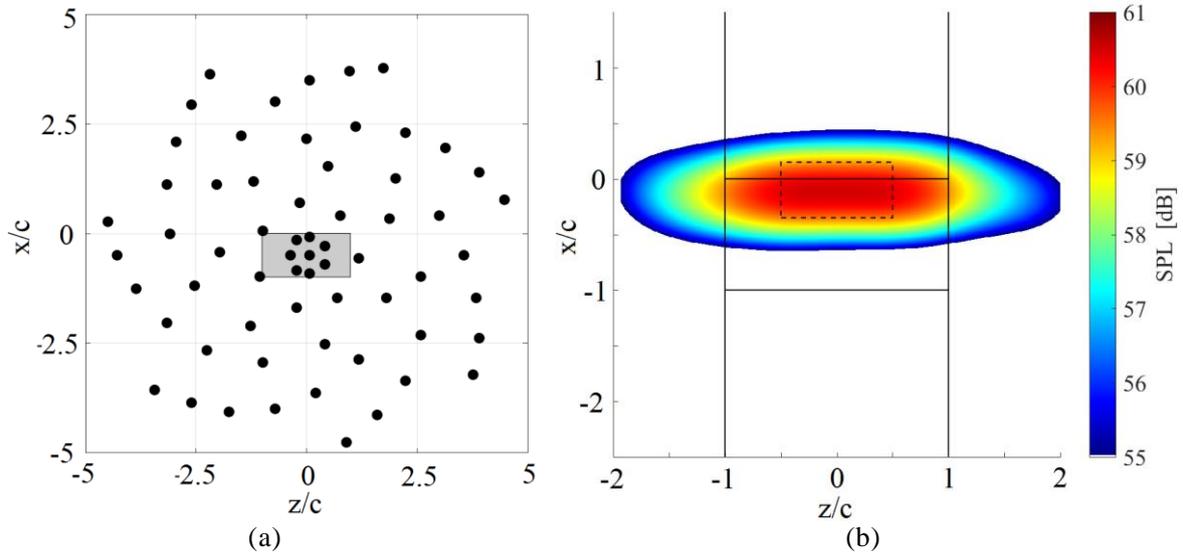
Figure 4 – (a) Distribution of the phased microphone array. Coordinates are shown in the airfoil system. The shaded area in grey represents the airfoil position with the flow direction in the positive x direction. (b) Source plot of the reference case ($U_\infty = 40$ m/s, $\alpha_g = 6°$) for the 1/3 octave band with center frequency at f=1.6 kHz

A sampling frequency of 50 kHz and a recording time of 60 s are used for each measurement. The acoustic data is separated in time blocks of 8192 samples ($\Delta t = 163.84$ ms) for each Fourier transform and windowed using a Hanning weighting function with 50% data overlap thus providing a frequency resolution of 6.1 Hz. The cross-spectral matrix (CSM) of the measured pressures is obtained by averaging the Fourier-transformed sample blocks over time. The expected error (16) in the estimate for the cross-spectrum is 5.2%.

Beamforming is performed on a square grid ranging between -2.5 < x/c < 1.5 and -2 < z/c < 2 and distance between grid points of 1 mm (figure 4 b). Conventional frequency domain beamforming (15) is applied to the acoustic data. Since trailing edge noise is a spanwise distributed sound source, integration of the source map in the range -0.5 < z/c < 0.5 and -0.35 < x/c < 0.15 (dashed box in figure 4 b) is performed (17-18). This method provided very satisfactory results for similar cases with simulated (19) and experimental (20) data.

5. RESULTS

5.1 Characterization of Porous Materials

5.1.1 Topology

2D microscopy images of the 3 metal foams used in the experiments are presented in figure 5. The images provide a representation of the inner topology of the foams that show a similar microstructure with porosity of approximately 90%. The basic cell shape is a dodecahedron with a cell diameter d_c approximately equal to the nominal cell diameter provided by the manufacturer (450, 580 and 800 μm), as shown in figures 5 (a), (b) and (c). On the other hand, the pore diameter d_p, i.e. the diameter of the faces of the dodecahedron, is approximately 3 or 4 times smaller. From a statistical investigation of the images it is found that the pore diameter is approximately 140, 170 and 220 μm for the three configurations respectively, as shown in figures 5 (d), (e) and (f).
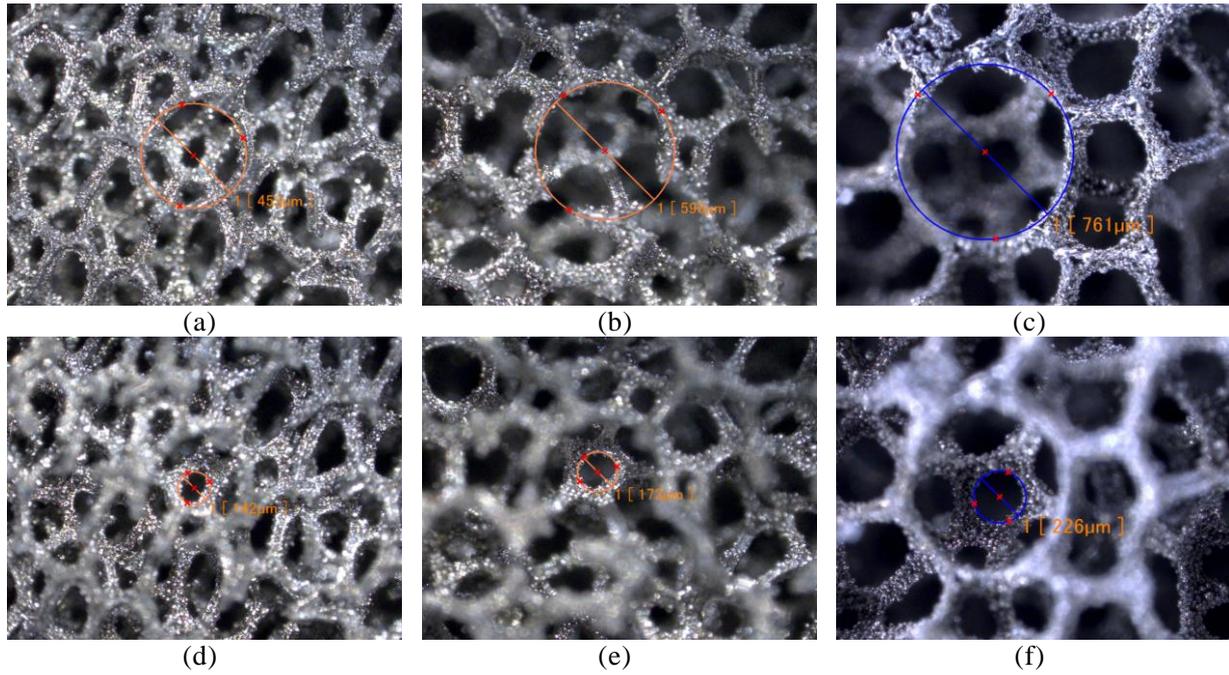
Figure 5 – View of the porous metal foams microscopic structure. From left to right, the images correspond to cell diameters of 450 μm, 580 μm and 800 μm respectively. The cell and pore diameters are focalized in the images (a), (b), (c) and (d), (e), (f) respectively.

Table 1 – Parameters characterizing the microstructure and the flow properties of the porous metal foams. Values in brackets are nominal values provided by the material supplier or estimated quantities.

d_c (μm)	d_p (μm)	φ (%)	R (N·s/ m^4)	K (m^2)	C (m^{-1})
(450)	(140)	89.28	29850	$6.11 \cdot 10^{-10}$	9758,24
(580)	(170)	90.46	10078	$18.10 \cdot 10^{-10}$	3052,70
(800)	(220)	91.65	6728	$27.10 \cdot 10^{-10}$	2612,54

5.1.2 Permeability and form coefficient

Figure 6 (a) shows the pressure drop for different sample thicknesses. For the sake of brevity, only the results for the metal foam with a nominal cell diameter of 450 μm are presented. Figure 6 (b) shows that the curves collapse for samples thicknesses larger than 30 mm. For smaller thickness the permeability of the foam is lower and the form coefficient is higher. A summary of the foam properties is reported in table 1.
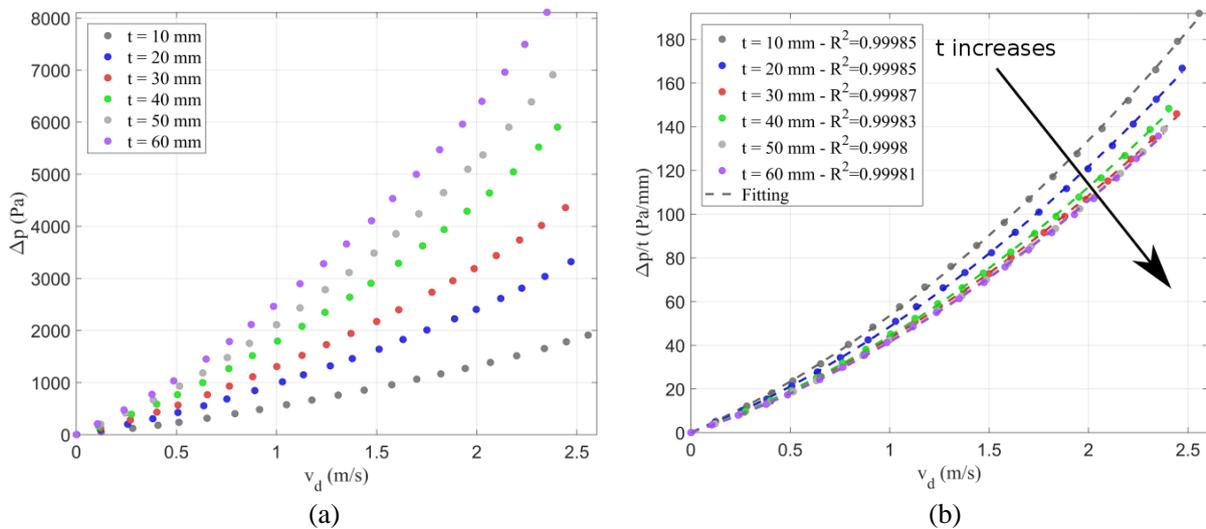
Figure 6 – Variation of the pressure drop across samples of the 450 μm cell diameter metal foam for different flow velocities. The tests have been performed on samples with thicknesses (t) ranging from 10 mm to 60 mm. (a) Measured pressure drop. (b) Measured pressure drop normalized by the thickness of the sample.

5.2 Static Pressure Distribution

The comparison between the measured differential pressure coefficient (ΔC_p) distribution along the chord of the airfoil for the solid trailing edge configuration is compared with the one obtained through XFOIL for $U_\infty = 20\ m/s$ and $U_\infty = 40\ m/s$ (figures 7 a, b) to assess the effective angle of attack. Such comparison shows that the geometrical angles of attack $\alpha_g = 0°,\ 6°,\ 12°$ correspond to free-stream angles of attack $\alpha = $ -0.3°, 3.5°, 6.8°, respectively. These results are within the uncertainty in measuring α_g, which is ±0.5°, and in line with the correction proposed by Brooks (1).
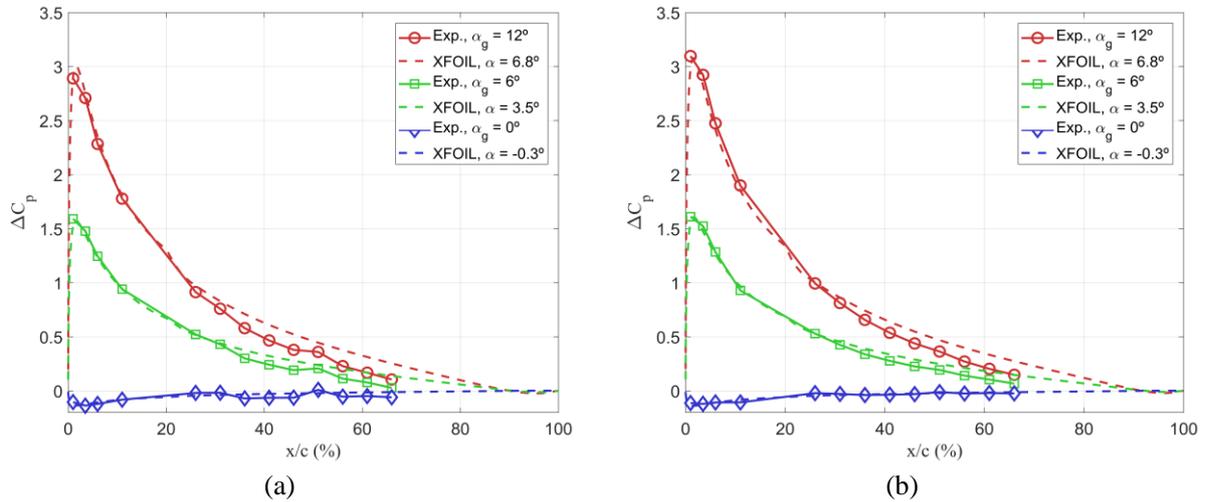
Figure 7 – Comparison between the measured pressure distribution and the one obtained through the vortex panel method code XFOIL. (a) $U_\infty = 20\ m/s$ (b) $U_\infty = 40\ m/s$.

The installation of the porous trailing edge does not introduce any upstream effect on ΔC_p as shown in figures 8 (a) and (b). No significant difference in the chord-wise differential pressure coefficient distribution is found with respect to the solid trailing edge. Since the use of a porous material does not alter significantly the pressure distribution upstream the porous insertion, the lift reduction in previous experiments (8, 9) might be caused by the modification of the static pressure distribution along the porous extent.
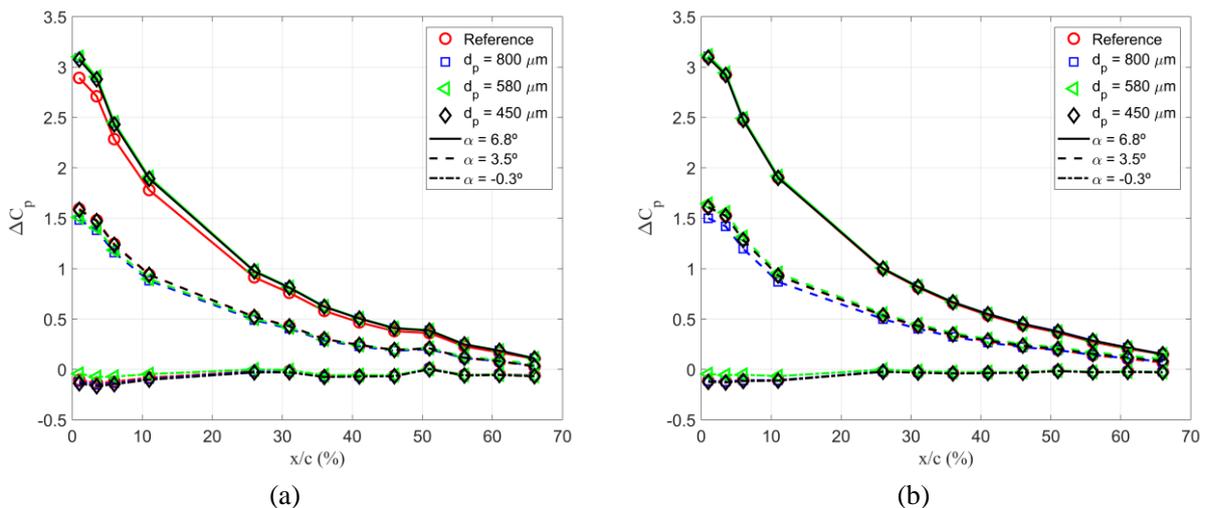
Figure 8 – Distribution of the difference between the suction and pressure side pressure coefficients along the chord of the airfoil. (a) $U_\infty = 20\ m/s$ (b) $U_\infty = 40\ m/s$. The porous extent covers 20% of the chord.

5.3 Acoustic Results

In the following, the results are presented in terms of $\Delta SPL_{1/3}$, which is defined as the difference between the Sound Pressure Level (SPL) of the solid trailing edge $SPL_{1/3}^{REF}$ and the partially porous one $SPL_{1/3}^{POR}$ (equation 5). Results are further averaged in the one-third octave band.

$$\Delta SPL_{1/3} = SPL_{1/3}^{REF} - SPL_{1/3}^{POR} \tag{5}$$

Thus, positive value denotes noise reduction with respect to the solid configuration.

5.3.1 Effect of the angle of attack

Figure 9 shows $\Delta SPL_{1/3}$ for the three investigated free-stream velocities and the three angles of attack for porous material length equal to 10% of the chord. All the porous materials show a common trend by varying the angle of attack. More in detail, increasing the angle of attack, $\Delta SPL_{1/3}$ decreases at lower frequencies while it increases at higher frequencies. As a consequence, when comparing the different angles of attack, a cross-over frequency is found (see dashed line in figure 9).
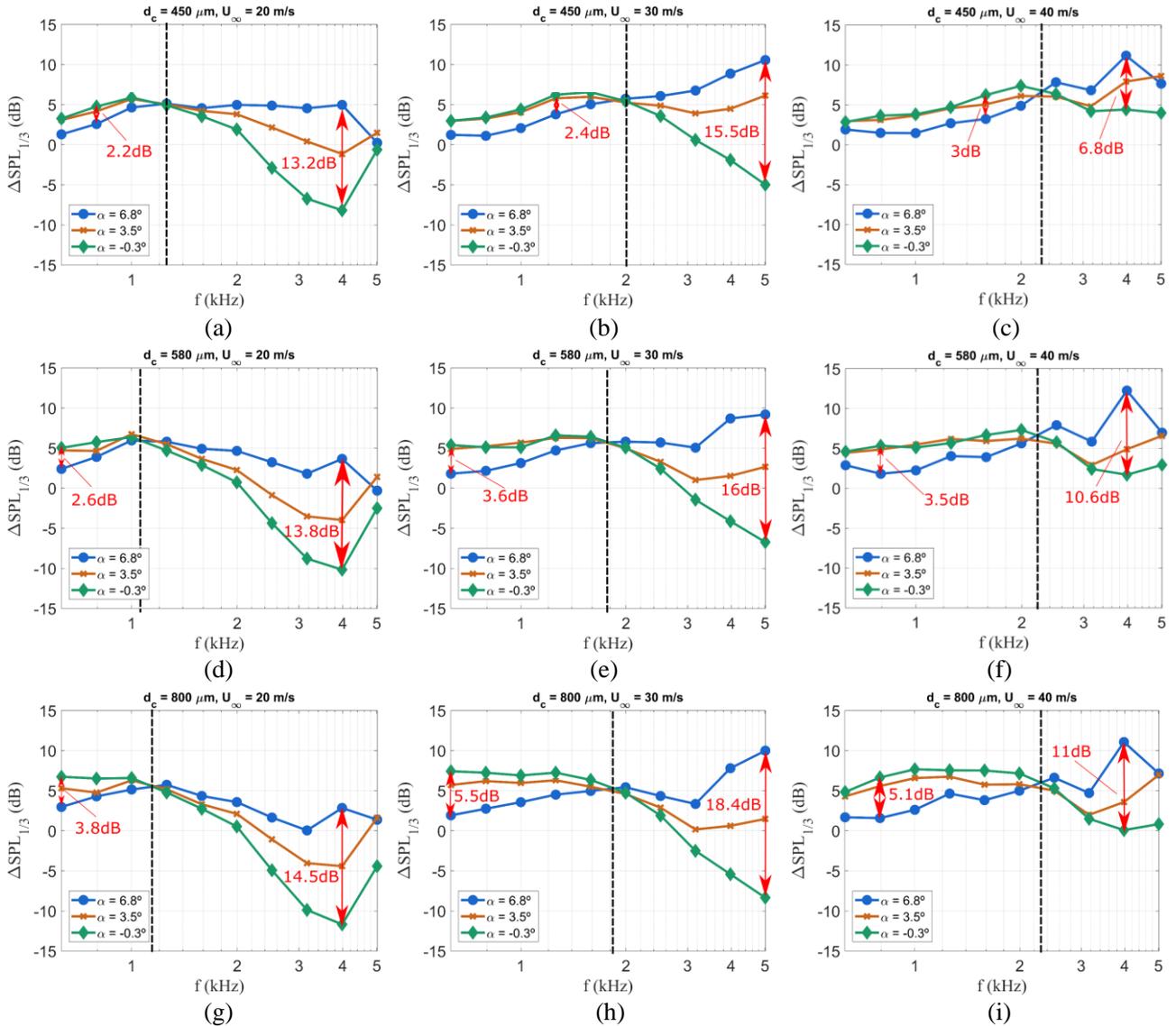
Figure 9 – Noise reduction due to the different metal foams used in the trailing edge at $U_\infty = 20\ m/s$ (left column), $U_\infty = 30\ m/s$ (middle column) and $U_\infty = 40\ m/s$ (right column). The results for metal foams with cell diameters of 800 μm, 580 μm and 450 μm, are presented in the bottom, middle and top rows, respectively. The porous extent covers 10% of the chord. Black dashed line indicates the cross-over frequency. The red arrows point out the maximum noise attenuation increase and decrease when α is increased from -0.3° to 6.8°.

A more detailed investigation of the results shows that, in the low frequency range, small differences are measured when varying the angle of attack. On the other side, large variations are

measured at higher frequencies. Furthermore, noise reduction is achieved for α = 6.8° over the entire range of measured frequencies, independently on the cell diameter or the velocity.

Increasing the cell diameter and the angle of attack, larger noise increase and reduction are measured at low and high frequency respectively. It is evident that, metal foams with the low flow resistivity and large cell size are more sensitive to variation of the angle of attack.

5.3.2 Effect of the porous extents

In figure 10, $\Delta SPL_{1/3}$ obtained for the porous metal foam with a cell diameter of 580 μm at the different angles of attack and velocities tested are presented for porous extent lengths equal to 10 and 20% of the chord.
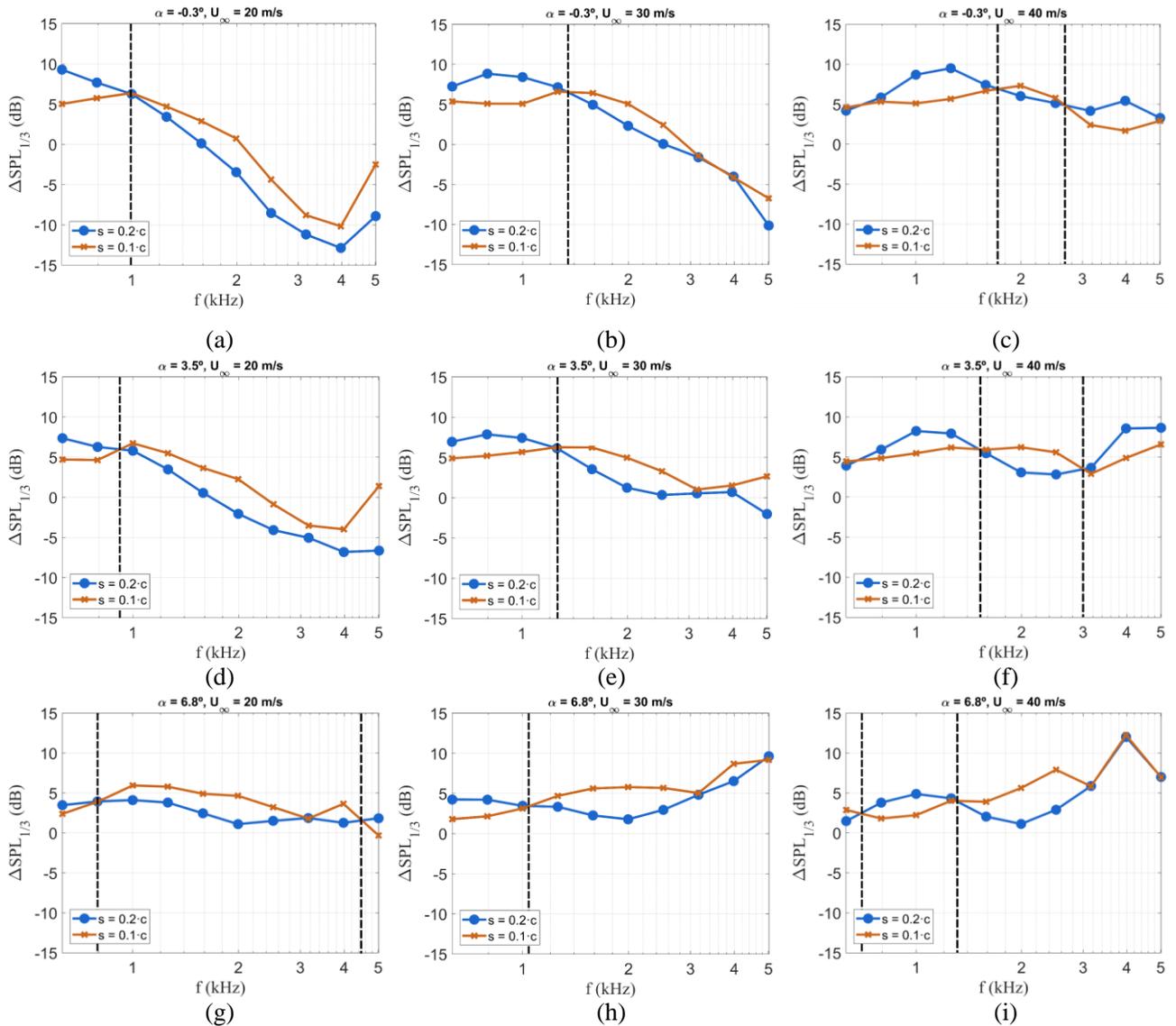
Figure 10 – Effect of using different porous extent lengths *s* of the 580 μm cell diameter metal foam on the noise attenuation for $U_\infty = 20 \ m/s$ (left column), $U_\infty = 30 \ m/s$ (middle column) and $U_\infty = 40 \ m/s$ (right column). Top, middle and bottom rows of plots contain data measured at $\alpha = -0.3°, \ 3.5°$ and $6.8°$, respectively. Circular and cross markers stand for porous insert length corresponding to the 20 and 10 % of the chord, respectively. Black dashed line indicates the cross-over frequency.

For a given angle of attack and free stream velocity, the effect of the length of the porous insert is frequency dependent.

In figure 10 (a) the noise attenuation for $\alpha = -0.3°$ at a velocity of 20 m/s is plotted. In this case, the use of a longer extent only implies further noise attenuation for frequencies below 1 kHz (this frequency is highlighted in the plot by a black dashed line). For the range of frequencies above this

limit the use of a longer extension decreases the noise attenuation. This fact might be associated to a longer rough surface. The increase of the angle of attack does not alter this behavior. In figure 10 (d), for the same free-stream velocity and a higher angle of attack ($\alpha = 3.5°$), the two aforementioned frequency ranges can be identified as well. Nevertheless, the limit between both ranges is now lower than in the previous case, i.e. approximately 900 Hz. This tendency is kept with further increase in the angle of attack. In figure 10 (g), the data measured at $\alpha = 6.8°$ show that the cross-over frequency is approximately 800 Hz. In this case, a third region at f = 5 kHz, in which the longer porous insert provides higher noise attenuation, appears.

The cross-over frequency is measured independently of the angle of attack. However, increasing the free-stream velocity, i.e. from 20 to 30 m/s, this frequency shifts to higher values. In figures 10 (b, e, h), corresponding to U_∞= 30 m/s, the cross-over frequencies are set to 1.34, 1.24 and 1.03 kHz for increasing angles of attack.

At $U_\infty = 40$ m/s, three different regions are found. In figures 10 (c, f, i), corresponding to $\alpha = -0.3°$, 3.5° and 6.8° respectively, it is shown that using a shorter porous extent length only generates higher noise attenuation in the mid-frequency range. At $\alpha = 6.8°$, the shorter insert also generates higher noise reduction for $f = 630$ Hz. In this case, since in the high frequency range ($f \geq 3.15$ kHz) both porous extents lengths generate similar results, the use of a larger porous area only produces benefits within $0.7 \leq f \leq 1.3$ kHz.

Although the results are not shown here for sake of brevity, the behavior described above for the metal foam with $d_c = 580$ μm is also present for the other tested metal foams.

6. CONCLUSIONS

In the present study, far-field noise measurements in presence of three different porous trailing edges retrofitted to a NACA0018 airfoil are performed. The effects of the angle of attack, free-stream velocity and the length of the porous insert on the far-field noise are studied.

The measurement of static pressure distribution up to 66% of the airfoil chord shows that the porous extent does not have any upstream effect on the pressure distribution. Thus, the lift reduction, reported in previous investigations, might be caused by the variation of the pressure distribution along the porous extent.

The acoustic measurements show that increasing the angle of attack decreases the noise attenuation with respect to the solid trailing edge at low frequencies, while it increases at higher frequencies. The cross-over frequency marking the separation between both frequency ranges does not depend on the angle of attack for a given free-stream velocity and cell diameter. The intensity of the attenuation also depends on the material; metal foams with lower flow resistivity and larger cell size are more sensitive to angle of attack variations.

Finally, the effect of the porous insert length is investigated. Also in this case, a cross-over frequency is found by varying the chord-wise extension of the porous trailing edge. For low free-stream velocities, the use of a longer porous insert causes higher noise reduction below the cross-over frequency. On the other hand, for low free-stream velocities and angles of attack, increasing the porous extent does not lead to additional noise attenuation above the cross-over frequency. At a higher velocity, two cross-over frequencies are found. In particular, the shorter insert reduces noise in the mid frequency range more effectively than the longer one.

Within the framework of these experiments, the flow-field in the suction side of the porous insert has also been monitored using time-resolved PIV. The analysis of this data-set is expected to provide further insight in the physical mechanisms leading to the noise reduction and explain its variation with some of the parameters described in the present manuscript, such as the angle of attack, the porous extent or the metal foam characteristics.

REFERENCES

1- T.F. Brooks, D.S. Pope, M.A. Marcolini. Airfoil Self-Noise and Prediction. NASA reference Publication; July 1989.

2- S. Oerlemans, P. Sijtsma, B. Méndez-López. Location and Quantification of Noise Sources on a Wind Turbine. J. Sound and Vibration; 2007.

3- A. L. Mardsen, M. Wang, J. E. Dennis, P. Moin. Trailing-edge noise reduction using derivative-free optimization and large-eddy simulation. J. Fluid Mech.; 2007.

4- C. Arce León, D. Ragni, S. Probsting, F. Scarano, J. Madsen. Flow topology and acoustic emissions of trailing edge serrations at incidence. Exp. in Fluids; 2016.

5- M. Herr, W. Dobrzynski. Experimental Investigations in Low-Noise Trailing Edge Design. AIAA Journal. Vol. 43; No. 6; June 2005.

6- M. Herr. Design Criteria for Low-Noise Trailing Edges; 13th AIAA/CEAS Aeroacoustics Conference (28th AIAA Aeroacoustics Conference); July 2007.

7- T. Geyer, E. Sarradj. Noise Generation by Porous Airfoils. Conference: 13th AIAA/CEAS Aeroacoustics Conference (28th AIAA Aeroacoustics Conference); July 2007.

8- T. Geyer, E. Sarradj. Trailing edge noise of partially porous airfoils. 20th AIAA/CEAS Aeroacoustics Conference; AIAA AVIATION Forum; AIAA 2014-3039; Atlanta, GA; June 2014.

9- M. Herr, K.S. Rossignol, J. Delfs, M. Möbner, N. Lippitz. Specification of Porous Materials for Low-Noise Trailing Edge Applications. 20th AIAA/CEAS Aeroacoustics Conference; AIAA AVIATION Forum; AIAA 2014-3041; Atlanta, GA; June 2014.

10- T. Geyer, E. Sarradj, C. Fritsche. Measurement of the noise generation at the trailing edge of porous airfoils. Exp. Fluids; 48:291-308; 2010.

11- D. B. Ingham, I. Pop. Transport Phenomena in Porous Media. Pergamon; September 1998.

12- E. Baril, A. Mostafid, L.P. Lefebvre, M. Medraj. Experimental Demonstration of Entrance/Exit Effects on the Permeability Measurements of Porous Materials. Adv. Eng. Mat. Volume 10; Issue 9; September, 2008

13- M. Drela. XFOIL: an analysis and design system for low Reynolds number airfoils. Conference on Low Reynolds Number Airfoil Aerodynamics, University of Notre Dame; 1989

14- J. R. Underbrink. Circularly symmetric, zero redundancy, planar array having broad frequency range applications. US Patent 6; 205; 224 B1; 2001.

15- T. J. Mueller. Aeroacoustic Measurements Springer Science & Media;2002; ISBN: 9783642075148

16- A. Brandt. Noise and vibration analysis: signal analysis and experimental procedures. John Wiley & Sons.

17- C. Arce Leon, R. Merino-Martinez, D. Ragni, F. Avallone, M. Snellen. Boundary layer characterization and acoustic measurements of flow-aligned trailing edge serrations. Experiments in Fluids; 2016.

18- C. Arce Leon, R. Merino-Martinez, D. Ragni, F. Avallone, F. Scarano, S. Pröbsting, M. Snellen, D. G. Simons, J. Madsen. Effect of trailing edge serration-flow misalignment on airfoil noise emission. Journal of Sound and Vibration; vol. 405; pp. 19-33; 2017; DOI: 10.1016/j.jsv.2017.05.035.

19- E. Sarradj, G. Herold, P. Sijtsma, R. Merino-Martinez, A. M. N. Malgoezar, M. Snellen, T. F. Geyer, C. J. Bahr, R. Porteous, D. J. Moreau, C. J. Doolan. A microphone array method benchmarking exercise using synthesized input data. 23rd AIAA/CEAS Aeroacoustics Conference; June 5-9 2017; Denver; CO; USA.

20- R. Merino-Martinez, W. C. P. van der Velden, F. Avallone, D. Ragni. Acoustic measurements of a DU96-W-180 airfoil with flow-misaligned serrations at a high Reynolds number in a closed-section wind tunnel. 7th International Meeting on Wind Turbine Noise; May 2-5 2017; Rotterdam, the Netherlands.